

Article

# A 4 mm Micro Servo Control System in Fiber Positioner

Shaoxiong Guo <sup>1,†</sup> , Yan Yang <sup>2,†</sup> and Chao Zhai <sup>3,\*</sup>

<sup>1</sup> Department of Precision Machinery and Precision Instrumentation, University of Science and Technology of China, Hefei 230026, China; gsx1998@mail.ustc.edu.cn

<sup>2</sup> School of Biomedical Engineering, Division of Life Sciences and Medicine, University of Science and Technology of China, Hefei 230026, China

<sup>3</sup> Experiment Center of Engineering and Material Science, University of Science and Technology of China, Hefei 230026, China

\* Correspondence: zhaichao@ustc.edu.cn

† These authors contributed equally to this work.

**Abstract:** As multi-object spectrographs (MOSs) continue to evolve, a notable trend has emerged—the increasing accommodation of fiber positioners on ever-more compact focal planes. This progression has seen the traditional stepper motors being supplanted by more space-efficient miniature hollow-cup motors. A significant challenge faced in the employment of these 4 mm diameter motors is the absence of compatible angle sensors, resulting in reliance on open-loop control methods for positioning. Addressing this challenge, this paper introduces a novel miniature angle sensor designed specifically for 4 mm hollow-cup motors, and presents a newly formulated closed-loop control scheme, which leverages this sensor to achieve accurate positioning. This marks the first implementation of an angle closed-loop control system within a 4 mm miniature hollow-cup motor used in MOS fiber positioners. Experimental evidence suggests that this sensed closed-loop mode substantially improves upon the energy efficiency and precision of fiber positioner placement, compared with traditional open-loop stepper control methods. Furthermore, the integration of these microsensors mitigates collision risks during the concurrent operation of fiber positioners by deactivating the motor power supply to prevent potential damage to the system.

**Keywords:** miniature hollow-cup motor; fiber positioner; multi-target fiber optic spectroscopic telescopes; astronomical spectroscopic technologies and instruments



**Citation:** Guo, S.; Yang, Y.; Zhai, C. A 4 mm Micro Servo Control System in Fiber Positioner. *Actuators* **2023**, *12*, 470. <https://doi.org/10.3390/act12120470>

Academic Editor: Micky Rakotondrabe

Received: 6 November 2023

Revised: 30 November 2023

Accepted: 13 December 2023

Published: 17 December 2023



**Copyright:** © 2023 by the authors. Licensee MDPI, Basel, Switzerland. This article is an open access article distributed under the terms and conditions of the Creative Commons Attribution (CC BY) license (<https://creativecommons.org/licenses/by/4.0/>).

## 1. Introduction

Fiber positioners are critical components in multi-object spectrographs (MOSs) [1,2]. These devices are precisely mounted on a telescope's focal plane board and are responsible for accurately aligning optical fibers at specific target points within the observational field. The fiber alignment allows for the collection of spectral data from a variety of astronomical sources [3–5]. Typically, thousands of positioners operate in concert [6], allowing for the simultaneous sampling of the light field emanating from multiple celestial bodies, thus markedly enhancing the throughput of spectroscopic surveys. While designs differ, fiber positioners generally fall into three primary categories:  $\theta$ -R,  $\theta$ - $\phi$ , and X-Y, as illustrated in Figure 1 [7]. These robotic arms are primarily actuated by stepper motors, brushless DC motors (BLDCMs), or piezoelectric ceramics, each suited to specific movement types.

Stepper motors and BLDCMs are generally associated with rotational movements and are commonly found in  $\theta$ - $\phi$  and  $\theta$ -R style positioners. Contrarily, piezoelectric ceramics, which induce translational motion, are utilized in X-Y style positioners. Positioners leveraging piezoelectricity often exhibit significant tilt inaccuracies due to the tip-tilt mechanism, which presents challenges in control precision and repeatability. Furthermore, these systems introduce complexities in devising anti-collision algorithms [8,9]. Nevertheless, they benefit from straightforward voltage-based control systems and the durability of

their solid-state structure, which can withstand substantial operational stresses. This is demonstrated by systems such as the fiber multi-object spectrograph (FMOS) [10] on the Subaru Telescope and the 4-m multi-object spectroscopic telescope (4MOST) [11].

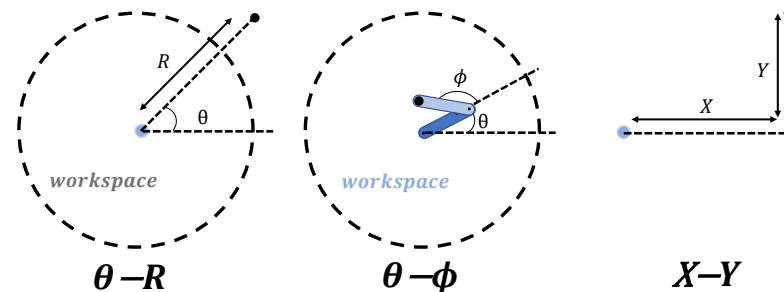


**Figure 1.** Three primary categories of fiber positioners.

While  $\theta$ - $R$  fiber positioners have been subject to initial research and small-scale testing, their deployment in fully operational telescopic assemblies remains limited. However, it is essential to note that the  $\theta$ - $\phi$  style positioners, propelled by electromagnetic rotary actuators, are currently the preferred choice for the majority of fiber positioning systems [12]. Prominent examples of their usage include the Multi Espectrógrafo en GTC de Alta Resolución para Astronomía (MEGARA) [13], the Dark Energy Spectroscopic Instrument (DESI) [14], the Large Sky Area Multi-Object Fiber Spectroscopic Telescope (LAMOST) [1], and the Multi-Object Optical and Near-infrared Spectrograph (MOONS) [15].

In the realm of rotary motors used as power sources, motor operation efficiency is a pivotal aspect to consider. The drive system's excessive power dissipation can induce temperature disparities, potentially giving rise to turbulent air currents adjacent to the focal plane board. These currents can have detrimental effects on the signal-to-noise ratio of the captured spectrum [16]. In light of ongoing advancements in multi-object spectroscopy (MOS), a clear shift has been observed from conventional, less efficient stepper motors to brushless direct current motors (BLDCMs), which offer superior efficiency. This transition is prominent in systems like DECI and the future iterations of LAMOST. Notably, the hollow-cup BLDCM can achieve reduced volume, exemplified by the smallest stepper motors such as those offered by Faulhaber, with diameters as small as 6 mm. Employing hollow-cup motors as actuators enables the creation of more compact fiber positioners, allowing for a denser placement of these positioners on a given focal plane board. This densification enhances the spectral data acquisition capacity, thereby elevating the efficiency of spectral surveys.

For the application of a fiber positioner, the use of highly compact microdrives is imperative. After extensive evaluation, a  $\phi 4$  mm hollow-cup motor, provided by NAMIKI Precision Jewel Co., Ltd., Tokyo, Japan, has been identified as the optimal choice. Table 1 delineates the motor's detailed specifications. The compact microdrive system is instrumental in ensuring stability and precision within the realm of micro-precision instrumentation. The primary subject of our investigation is the 4 mm motor, whose structural components are depicted in Figure 2. The key features of the motor's construction are as follows:

- (1) The stator winding consists entirely of self-supporting copper coils arranged in a skewed pattern, as opposed to coils wound on a laminated iron core. This innovative coreless stator design is lightweight and devoid of cogging torque, which enhances its performance.
- (2) The motor's compact architectural design incorporates an internal rotor that is a singular cylindrical permanent magnet, magnetized in the diametrical plane. This feature results in low rotational inertia and high responsiveness to changes in rotational speed.

**Table 1.** Hollow-cup motor parameter.

BMN04-8	Value	Unit
Pole pairs	1	
Rated speed	617	Hz
r (single-phase resistance)	14.85	$\Omega$
Ls (coil inductance)	37	$\mu\text{H}$
Ld (inductance of d axis)	37	$\mu\text{H}$
Lq (inductance of q axis)	37	$\mu\text{H}$
Ld/Lq ratio	1	
BEMF constant	0.059	mV/rpm
Inertia	0.00087	$\text{g cm}^2$

The efficiency of a motor's operation, which can impact its environmental interactions, indirectly influences observational outcomes, while the motor's positioning accuracy directly affects the light throughput. For systems such as MOONS and MEGARA, which lack an integrated visual feedback mechanism for monitoring fiber positioning during telescope observations, there is a critical need for robust absolute open-loop accuracy. In contrast, sophisticated systems like LAMOST, DESI, Sloan Digital Sky Survey V (SDSS-V) [17], and Subaru employ dedicated feedback architectures that incorporate visual servoing, enhancing fiber positioning accuracy through iterative imaging using their visual systems [18]. The required number of imaging iterations varies depending on the precision needed for positioning and the complexity of the astronomical object being observed. Nevertheless, all systems aspire to achieve optimal positioning performance, even in the absence of visual feedback, to minimize the necessity for visual iterations, thereby reducing positioning time and enhancing the system's observational efficiency.

In the context of motor position acquisition, sensorless control methods have been at the forefront of research for many years. Particularly noteworthy at zero and low speeds are high-frequency injection (HFI) methods RN1105. The historical development of these methods includes rotational sinusoidal voltage injection [19,20], pulse sinusoidal voltage injection [21,22], and pulse square-wave voltage injection [23,24]. These methods have made significant contributions to the advancement of sensorless control in low-speed conditions. For zero and low-speed operations, sensorless control utilizing HFI can be implemented by leveraging the salient characteristics of permanent magnet synchronous motors (PMSMs). HFI techniques are dependent on magnetic anisotropies [25]: The stator coil inductance undergoes changes in response to the rotor permanent magnet position. These variations in inductance produce distinct reactance when high-frequency voltage is applied, resulting in unique current responses. By harnessing these differential current signatures, the high-frequency component—distinct from the fundamental frequency of motor rotation—can be isolated. Subsequently, the rotor position angle can be inferred. This effect exploits the salient-pole feature of the motor. However, the magnetic circuit of a hollow-cup motor demonstrates pronounced isotropy for the following reasons:

- (1) The magnetic circuit structure of the rotor's d-axis and q-axis are uniform and exhibit no saliency.
- (2) Due to the absence of an iron core in the coil, the magnetic reluctance is high. The inductance of the winding, resistant to saturation, maintains a wide operating bandwidth and hence exhibits no saturation saliency.

Consequently, sensorless methods that rely on magnetic circuit anisotropies are not suited for the specified 4 mm motor. Moreover, regardless of whether they are based on saliency [26], back electromotive force (Back-EMF) [27], or magnetic flux linkage [28], sensorless methods have primarily been documented for use in speed control applications (such as fans, pumps, and propellers), and they have limited suitability in precision positioning tasks. Therefore, sensed control methods have become the predominant approach.

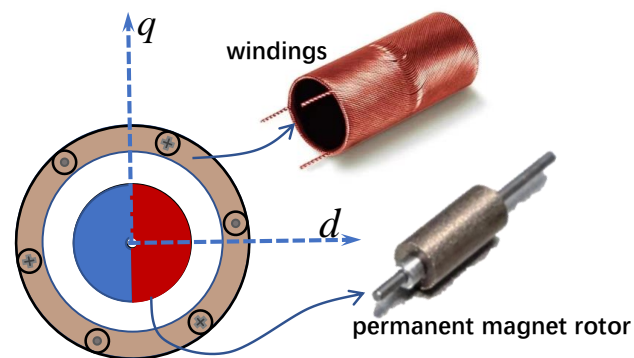


**Figure 2.** Structure of miniature-sized hollow-cup motor.

Nevertheless, a lacuna persists in the present market regarding suitable encoder solutions for 4 mm miniature hollow-cup BLDCMs designed for fiber positioners. Additionally, motor suppliers lack planning and layout in this specific field. To address this issue, and ensure the seamless integration of the 4 mm miniature hollow-cup motors within fiber positioning apparatuses, the research team designed a miniature sensor at the rear end of the motor shaft. This design aims to first achieve angular closed-loop vector control of the miniature hollow-cup motor in a fiber positioner. Concomitant with this design, our team further explored the specific impact this micro servo system brings to the fiber positioner.

Nevertheless, the marketplace still exhibits a gap in the availability of appropriate encoder solutions for 4 mm miniature hollow-cup BLDC motors tailored for fiber positioners. Additionally, motor suppliers have not adequately ventured into this niche area. To bridge this gap, and ensure the effective implementation of 4 mm miniature hollow-cup motors within fiber positioning systems, our research group has developed a miniature sensor to be mounted at the rear end of the motor shaft. The primary objective of this design is to facilitate angular closed-loop vector control of the miniature hollow-cup motor within a fiber positioner. Alongside this innovation, we have also examined the specific impact that this micro servo system has on the performance of the fiber positioner. The structure of this paper is organized as follows: Section 2 addresses the developmental methodology of the micro angle sensor, delineating aspects of simulation and magnetic system validation. The design of an inner-loop control strategy tailored to the micromotor's attributes is elucidated in Section 3, predicated upon voltage amplitude modulation within an open-loop system paradigm. Comparative analyses concerning the micro magnetic encoder's impact upon the fiber positioner in terms of both energy efficiency and precision in positioning are presented in Sections 4 and 5. Furthermore, Section 6 offers additional discussions on related topics.

## 2. Motor Magnetic Encoder System Design

The design of contactless miniature angle sensors often hinges on detecting the sinusoidal variations in the magnetic field across the air gap of a diametrically magnetized magnet, employing technologies such as magnetoresistive or Hall elements (as shown in Figure 3). Our developed contactless angle sensor system utilizes the MA735 (produced by Monolithic Power Systems, Inc., San Jose, CA, USA), which boasts an exceptionally compact footprint of just 2 mm by 2 mm, thus satisfying the stringent miniaturization criteria for sensor devices. The MA735 features vertical Hall elements to monitor the magnetic flux density in the direction of  $\vec{B}$ , with the objective of determining the rotor's angular position. It precisely registers the magnetic field components  $B_x$  and  $B_y$ , from which the rotation angle  $\alpha$  is derived using the arctangent function,  $\alpha = \text{atan2}(B_y, B_x)$ .

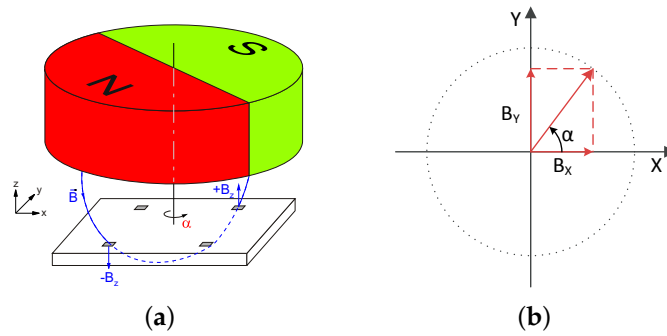


**Figure 3.** The principle of angle detection using vertical Hall device. (a) Vertical Hall sensor locations and measurement configuration. (b) Internal signals of Hall sensors.

To gain a comprehensive understanding of the properties of the magnetic air gap, a three-dimensional model of a cylindrical permanent magnet was developed. This model features a diameter of 2 mm and a height of 1.5 mm, with the magnetization oriented diametrically (aligned with the positive Y-axis) and simulated using ANSYS Maxwell. The magnet is composed of N42 material, boasting a remnant flux density in the range from 1280 mT to 1320 mT and a coercive force of  $923 \text{ kA m}^{-1}$ . Figure 4a,b display the spatial distribution of the total magnetic flux density, denoted as  $\vec{B}$ . Figure 4c provides a visualization of the Y-axis component of the magnetic flux density,  $B_y$ , specifically within the XZ plane. It is apparent from Figure 4d that  $B_y$  diminishes progressively as the size of the working air gap increases. Moreover, Figure 4e delineates the detailed attenuation trend across an air gap ranging from 0 mm to 3 mm.

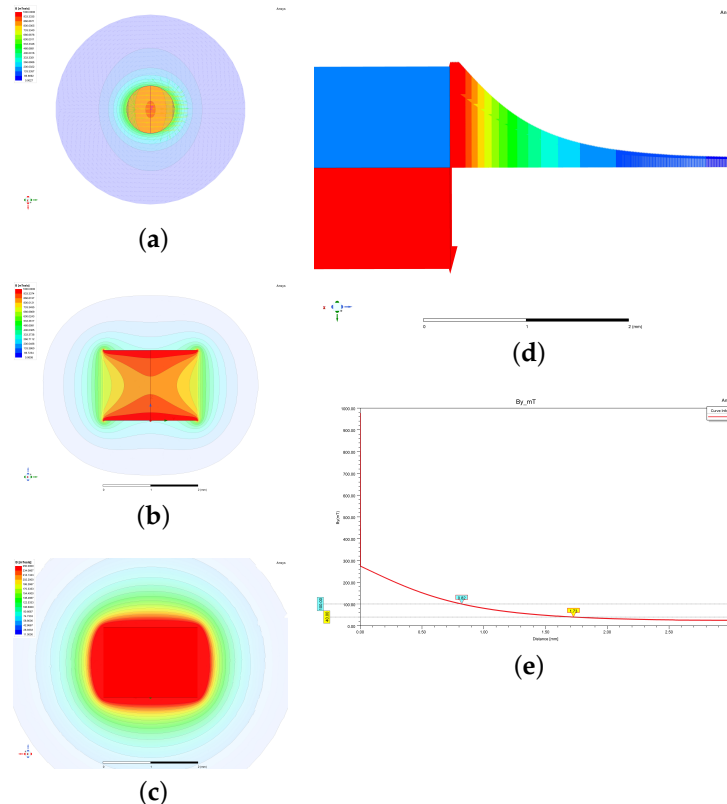


**Figure 4.** Air gap magnetic field distribution. (a) XY cross-section. (b) YZ cross-section. (c) Variation in  $B_y$  distributed in the XZ plane. (d) Attenuation of  $B_y$  along the Z-axis. (e) Air gap from 0 mm to 3 mm.

In Figure 4e, the attenuation profile of the magnetic field can be decomposed into two distinct behaviors, as depicted in Figure 5a,b. The former illustrates a rapid linear decrease in the  $B_y$  component of the magnetic field across the air gap, while the latter demonstrates a slower, nonlinear decay of its amplitude. Notably, Figure 5b exhibits a gradual decline in  $B_y$ , with its slope diminishing as the air gap width increases. The operational magnetic field strength for the sensor chip falls within this nonlinear decay phase, specifically between air gap values from 0.82 mm to 1.73 mm, as evidenced by Figure 5b.

This behavior is advantageous in real-world applications, offering tolerance for amplitude variations of  $B_y$  due to potential mechanical installation errors. In the experimental setup, custom-engineered sintered NdFeB magnets, aligned with the simulation parameters, were affixed to the rear shaft of the motor. With the aid of a one-dimensional precision micro-adjustment platform, the magnet was systematically displaced away from the magnetic chip in increments of 0.01 mm. Following each adjustment, the register value indicative of the magnetic field strength was captured, forming the basis for the graphical representation in Figure 5c. Notably, as the micro-adjustment platform shifts, the register lacks the precision to accurately quantify the field strength and instead provides comparative data that are indicative of whether the field strength is above or below a specified threshold. Hence, at a given position, the register can assert that the value of  $B_y$  lies within the range demarcated by the horizontal coordinates associated with the red and green markers in Figure 5c. This information is deemed sufficient for determining the appropriate air gap installation parameter.

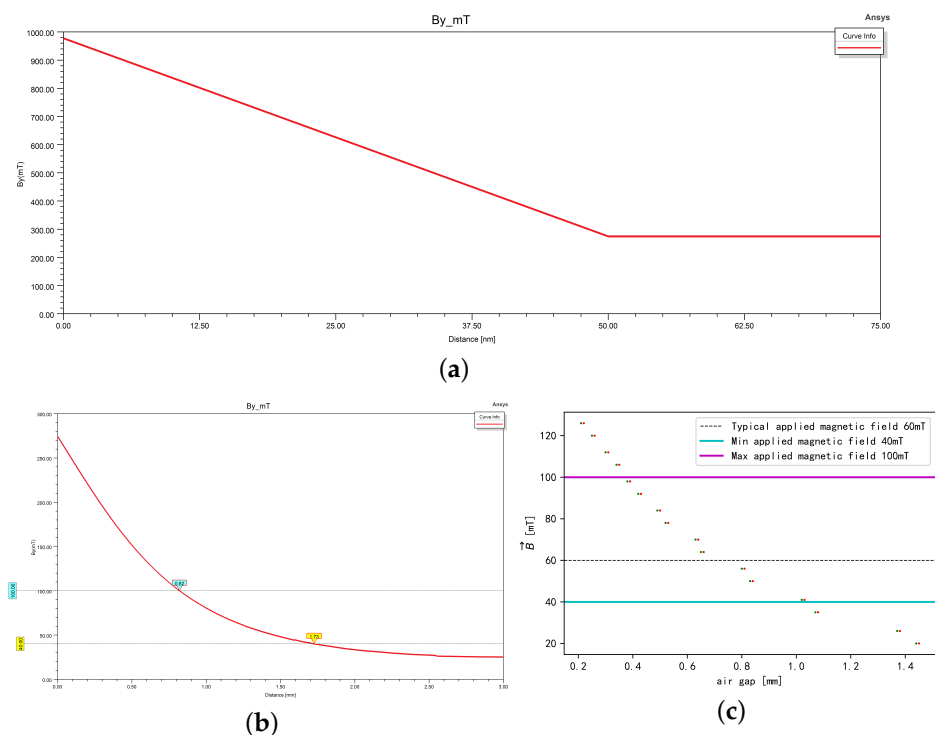


**Figure 5.** Attenuation of  $B_y$  with air gap variation and actual results. (a) Air gap within 0 nm to 75 nm. (b) Air gap from  $75 \times 10^{-6}$  mm to 3 mm. (c) Test results.

The specification manual for the MA735 model stipulates a prototypical value of the magnetic flux density,  $B_y$ , at 60 mT. The analysis of Figure 5c reveals that the actual operational air gap is approximately 0.7 mm for this specific field strength. When this observation is considered in conjunction with both Figure 5b,c, the rapid spatial attenuation of the magnetic field becomes apparent for a magnet of miniature dimensions, namely a radius of 1 mm and a height of 1.5 mm. Ansys Maxwell simulations predicted the air gap values that correlate with  $B_y$  at 40 mT and 100 mT to be 1.73 mm and 0.82 mm,

respectively. However, empirical measurements indicated significantly fewer air gaps, specifically 1.05 mm and 0.4 mm. This discrepancy suggests a more rapid degradation of the magnetic field intensity within the air gap post-manufacturing, which surpasses the decay rates assumed in the simulations. Consequently, it is deduced that the field strength attenuates to nullity at a distance of 2 mm to 3 mm from the magnet surface. In practical applications, for example, when deploying such miniature magnetic systems in densely populated fiber positioners on a focal plane array, it becomes evident that the magnetic interference between adjacent units is negligible.

### 3. Servo Control Loop Design

The frequency domain representation for the mathematical model of a direct current (DC) motor is expressed as follows:

$$V(s) = rI(s) + sLI(s) + e(s). \quad (1)$$

Here,  $e(s)$  denotes the Back-EMF. By applying the small-signal model to Equation (1), and considering that the variations in Back-EMF due to mechanical dynamics are considerably slower than the electrical time constant, the Back-EMF can be approximated as a constant value. This simplification leads to the following relations:

$$\begin{aligned} V_0 + \delta V &= (r + Ls)(I_0 + \delta I) + e_0 \\ \Rightarrow \delta V &= (r + Ls)\delta I \\ \Rightarrow \frac{I(s)}{V(s)} &= \frac{1}{r + Ls} \end{aligned} \quad (2)$$

For an ideal DC motor, torque is directly proportional to the current. Furthermore, assuming that the motor's inertia remains constant, the acceleration can be considered directly proportional to the current as well. This forms the basis for using a current loop to emulate an acceleration loop, which is typically foundational within control systems. The integration of acceleration over time yields velocity; therefore, by modulating the current, one can exert precise control over the velocity. Additionally, the cumulative integration of velocity corresponds to the displacement, facilitating position control via velocity modulation.

Incorporating the parameters specific to the hollow-cup motor into Equation (2) produces

$$\frac{I(s)}{V(s)} = \frac{1}{14.85 + 37 \times 10^{-6} \cdot s}. \quad (3)$$

The step response corresponding to Equation (3) is depicted in Figure 6a.

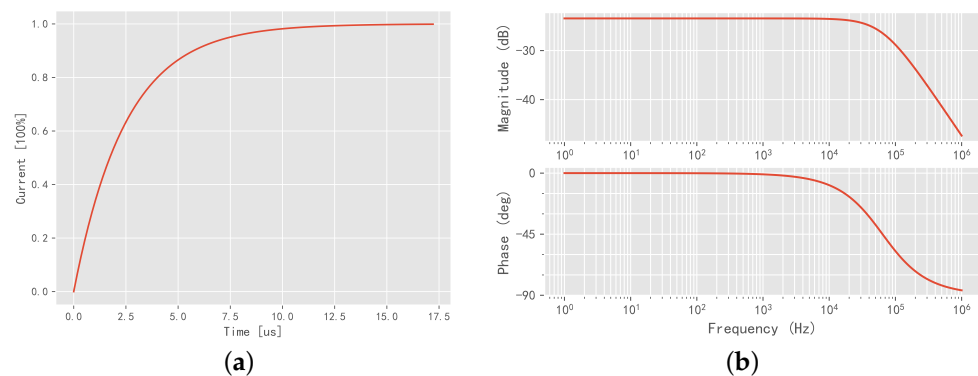


**Figure 6.** Time-domain and frequency-domain response characteristics of the motor. (a) Step response. (b) Magnitude-frequency and phase-frequency response.

The time taken for the current response to reach 63.2% of its steady state is merely 2.47  $\mu\text{s}$ , indicative of its remarkably swift nature. This rapidity is attributable to the high cutoff frequency inherent to Equation (3), resulting in a reduced response time. The Bode plot with detailed magnitude and phase–frequency response features is presented in Figure 6b.

The Namiki 4 mm micro hollow-cup motor’s rated speed is specified in the manual as 37,000 rpm. This motor has a single pair of poles, which translates into an electrical frequency of 617 Hz. In synchronous motor operation, there exists a fixed synchronization between the electrical frequency and the phase current frequency. When operating near the rated speed, negligible deviations occur in the current magnitude or phase response, as shown in Figure 6b. This phenomenon indicates that frequency variations have an inconsequential effect on the current response when the motor operates below its rated speed, validating the exclusion of frequency fluctuations from critical consideration in these conditions.

Motor control architectures customarily integrate a negative feedback loop for current regulation, primarily due to the phase angle by which the voltage precedes the current in inductive motor circuits. With the rise in electrical speed, this phase lead increases. Consequently, a negative feedback loop is crucial for maintaining precise control over the current’s magnitude and phase, which directly influences torque regulation—maintaining a 90° lead in the stator’s magnetic flux relative to the rotor’s magnetic flux ensures optimal efficiency from the current’s work output. In addition, typical iron-core BLDCMs have substantial inductance values and thick winding copper wires, leading to a larger electrical time constant typically in the millisecond range. The stator impedance is low, resulting in substantial currents through the windings. The use of a current feedback loop mitigates the risk of transistor failure due to overcurrent, thereby preventing potential safety hazards associated with Mosfets/IGBTs (insulated-gate bipolar transistors) operating under significant voltage endurance.

However, in the case of the  $\phi 4$  mm micromotor circuit model, the motor’s resistive properties considerably outweigh its inductive properties. At certain operational speeds, the inductive load imparts an imperceptible impact, as noticeable both in amplitude and phase responses. For our fiber positioner application, the motor’s operation will not reach this critical speed mark, which positions the motor firmly in the “resistive” category. Consequently, we can forgo the traditional current feedback loop and instead apply a voltage-based feed-forward control strategy. This approach leads to an open-loop control system focused on voltage amplitude without reliance on feedback mechanisms.

The architecture of the control algorithm within the microcontroller unit (MCU) for the servo loop is illustrated in Figure 7. The position loop is initiated by the timer update interruption at a frequency of 10  $\mu\text{s}$ . During each cycle, the trajectory planning module computes the desired position target angle  $\theta^*$ , and this value is then subtracted from the actual rotor angle  $\theta$ , as measured by the magnetic encoder. The resulting error signal is processed by a proportional–integral–derivative (PID) controller within the position loop to determine the appropriate  $V_q$ . Concurrently, the inner voltage loop is executed in a while-loop configuration, with a period of 2  $\mu\text{s}$ . This inner loop, which is designed to operate independently of current sampling, continuously retrieves the current rotor angle and generates a voltage vector with a 90° phase lead with respect to the rotor angle. This mechanism is essential for the closed-loop control of the phase angle. The amplitude of the voltage vector, which is informed by the  $V_q$  output of the position loop, is held constant throughout the execution of the voltage loop to maintain amplitude control in an open-loop manner. Additionally, the implementation of a pulse width modulation (PWM) carrier frequency as high as 500 kHz aids in more effective filtering by the RL low-pass circuit, reducing interference from the carrier frequency in the modulated sinusoidal signal, and ensuring the integrity of the sinusoidal modulation of the current.

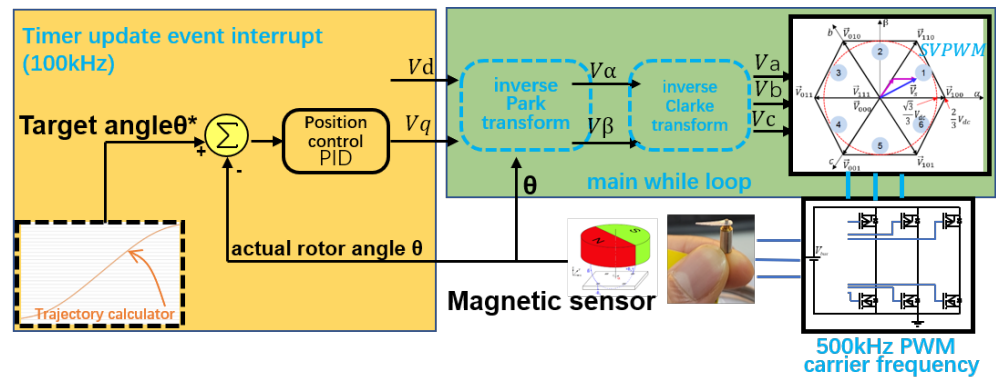


Figure 7. Servo control logic.

#### 4. Dynamic Power Consumption Testing

Figure 8b presents the setup for the 4 mm micro servo motor, positioned in the upper-right corner, with the magnetic encoder chip affixed to a  $\phi 3.4$  mm printed circuit board (PCB). A custom motor with an extended shaft is employed in this configuration. The integration of the micro-PCB and magnet is achieved using precision 3D-printed components, with the design meticulously tailored to maintain a precise installation gap of 0.7 mm (refer to Section 2 for details). However, for the eccentric shaft motor embedded in the internal structure of the fiber positioner, it is unfeasible to install the encoder in this way. Therefore, the described microsensor system is exclusively applied to the central shaft motor configuration.

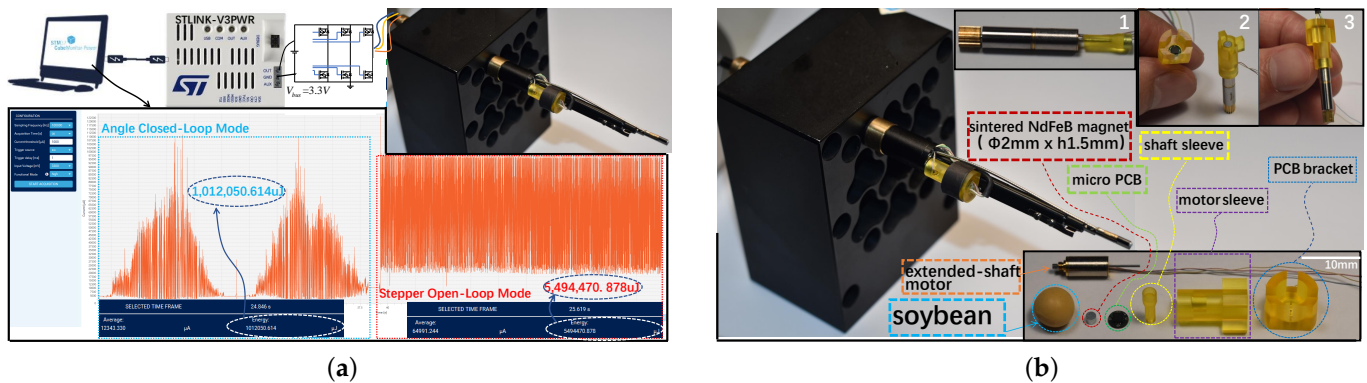


Figure 8. Dynamic power consumption test. (a) The comparative analysis of dynamic power consumption between angle closed-loop and stepper open-loop systems. (b) Components and installation of the angle sensor system.

To evaluate the dynamic power consumption of the motor across varied driving modes whilst handling an equivalent load, the STLINK-V3PWR hardware platform is utilized. It supplies power to the central shaft motor and measures its dynamic power consumption during operation. Data acquisition and analysis are conducted using the STM32CubeMonitor-Power software tool. The STLIN-V3PWR is adept at measuring currents across peak modes ranging from 0.1 mA to 50 mA, 0.3 mA to 150 mA, 0.6 mA to 300 mA, to 500 mA. The device is also capable of executing low-power sampling with an accuracy of 2%, within the power range from 0.16 W to 1.65 W, and at sampling rates up to 100 kSps. As such, the STLINK-V3PWR is particularly suited for the dynamic power analysis of micro hollow-cup motors. As depicted in Figure 8a, the driving circuit for the three-phase full-bridge motor is powered by a 3.3 V DC supply, delivered by the STLINK-V3PWR. This device enables the monitoring of the dynamic power consumption of the motor and its driving circuit at the supply rail, allowing for the isolation of dynamic

and static power usage from other system components. During operation, the central shaft is instructed to execute a full rotational cycle in both directions, employing both sensed closed-loop and sensorless stepper modalities. A power meter records the power consumption for the entire cycle.

In the sensed closed-loop mode, which incorporates acceleration and deceleration phases, the dynamic power consumption traces a distinctive “mountain” pattern. When comparing forward and reverse rotations, the power profiles are correspondingly similar in this mode. In stark contrast, employing a sensorless open-loop control—which maintains the robustness characteristic of open-loop systems as outlined by previous research [29]—involves a uniform-speed stepping approach. Here, the dynamic power consumption assumes a “rectangular” profile. For identical one-revolution tasks in both directions, the sensed mode demonstrates superior energy efficiency, consuming 1,012,050.614  $\mu\text{J}$ , which is a mere 18.42% of the 5,494,470.878  $\mu\text{J}$  expended in sensorless stepper mode. This pronounced difference highlights the energy-saving benefits of sensor-assisted driving methods.

### 5. Fiber Alignment Accuracy Test

To assess the positional accuracy of different drive modes within an actual telescope’s visual servo system, the illustrated visual measurement system in Figure 9 serves as the cornerstone for carrying out visual servo positioning tasks. The complete setup is anchored to a precision platform. Employing the same telephoto lens as used in an astronomical observatory—characterized by minimal distortion—the visual measurement system in the laboratory is positioned on a horizontal slide to enable movement in the X direction. The fiber positioner, with its installation base, allows for precise adjustments in the Z axis and translational movement along the Y axis. Fine-tuning the slide’s position ensures that the fiber’s ceramic tip remains within the camera’s viewing range.

Once light is supplied to the fiber through a rear-integrating sphere and subsequently emitted at the tip, the camera takes an image to capture the resultant bright circular spot. These images are utilized to ascertain the fiber’s absolute position following each positioning operation. By calculating the point-to-point discrepancy, instructions for the impending motor drive sequence are generated. This iterative correction process, performed by the visual system, generally requires four cycles to achieve the desired accuracy for a targeted position. The locations within the inspection domain of the fiber positioner are generated via a stochastic algorithm.

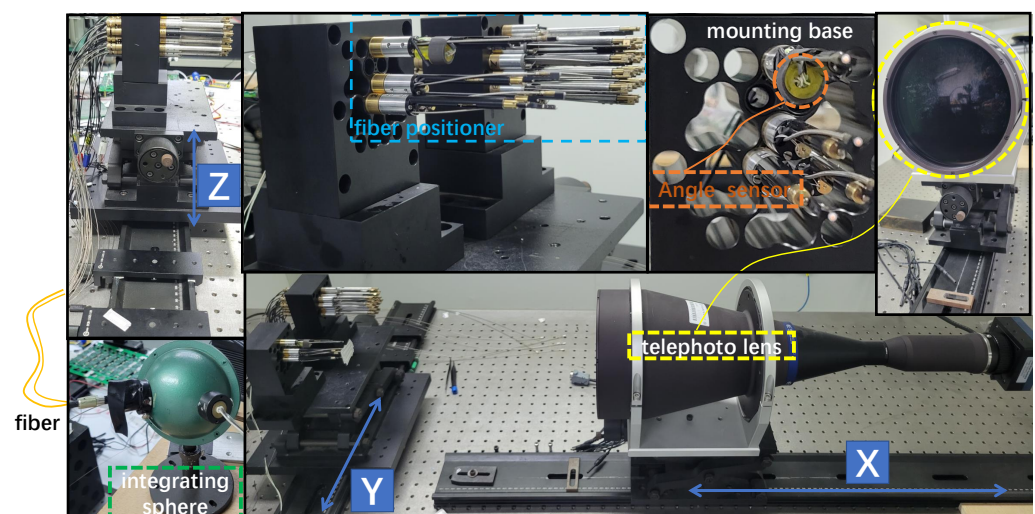
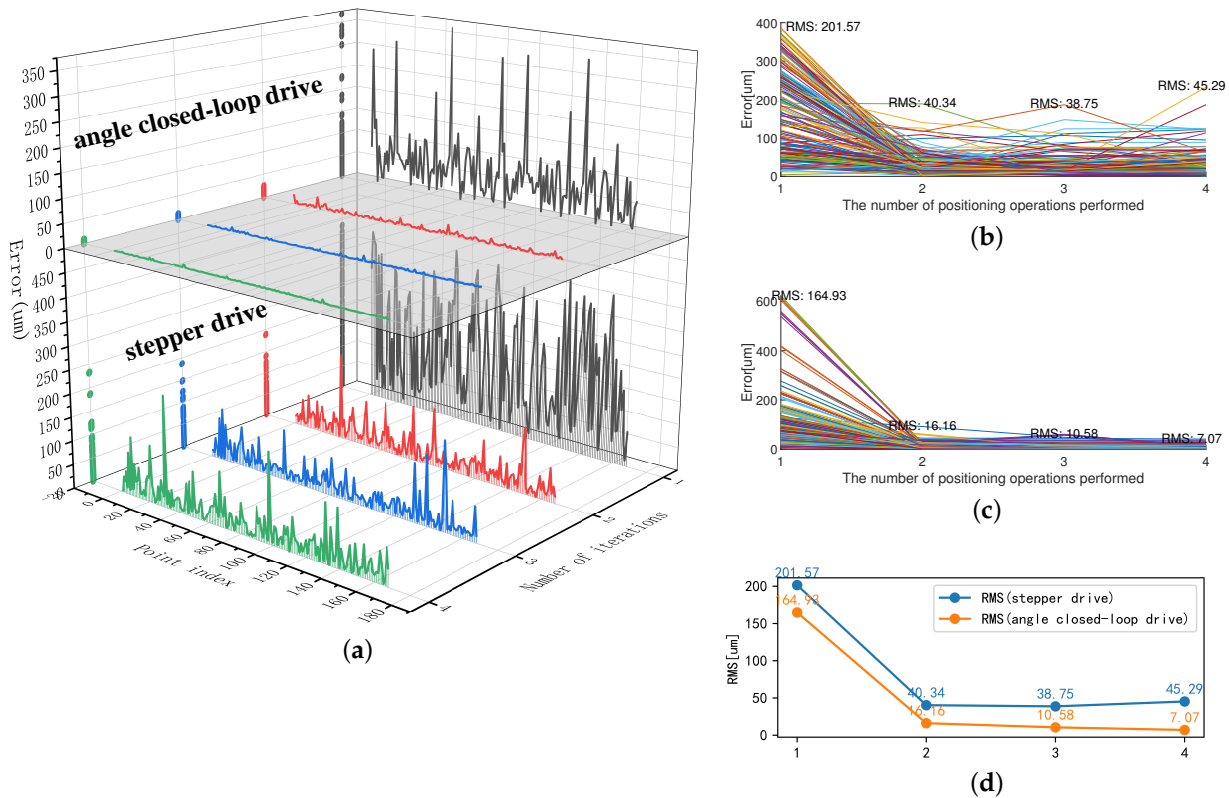


Figure 9. Visual measurement system.

In this experiment, the central shaft motor of a single fiber positioner is operated in both stepper mode and closed-loop mode with sensor feedback, while the eccentric shaft motor is maintained exclusively in stepper mode. The performance of the fiber positioner is empirically evaluated by directing it to attain 168 randomly designated points in both operational modes. The results obtained from these tests are graphically depicted in Figure 10.



**Figure 10.** The positioning results of the fiber positioner after four iterations. (a) Three-dimensional waterfall plot of convergence of errors. (b) The results of the fiber location under the stepper drive of the central axis motor. (c) The results of the fiber location under angle closed-loop drive of the central axis motor. (d) Comparison of RMS errors.

In Figure 10a, the 3D waterfall plot illustrates the error distribution after four iterations under both open and closed-loop controls. Under angle closed-loop control, the fiber positioning error in each individual iteration shows superior results compared to open-loop control. Furthermore, the closed-loop mode exhibits overall better convergence characteristics. Figure 10b,c meticulously present the dynamic iterative convergence process for all positioning points. Figure 10d depicts the dynamic variation in RMS values over the four iterations. The RMS values within the closed-loop consistently outperform those in the open-loop, and it is noteworthy that, in the open-loop mode, the RMS value in the fourth iteration exhibits a slight divergence compared to the previous three iterations. In contrast, under closed-loop control, the RMS values consistently demonstrate a converging trend with an increasing number of iterations.

Figure 10b,c offer a detailed examination of the dynamic iterative convergence process for all target positions. Figure 10d illustrates the dynamic changes in root mean square (RMS) error values across the four iterations. The RMS error values associated with the closed-loop mode are consistently lower than those linked with the open-loop mode. Significantly, during the fourth iteration under the open-loop mode, the RMS value exhibits a marginal increase, indicating a slight divergence from the decreasing trend observed in

the preceding iterations. In stark contrast, closed-loop control demonstrates a consistent and progressive decline in RMS values as the number of iterations increases.

The evidence clearly suggests that the implementation of sensor-based closed-loop control for the central shaft motor considerably enhances the iterative positioning accuracy and overall convergence of the fiber positioner. In contrast, the stepper mode of operation subjects the system to the risk of step loss, thereby introducing additional unpredictability into the operational fidelity of the fiber positioner.

## 6. Discussion

Table 2 consolidates data on the characteristics of actuators in widely used  $\theta$ - $\phi$ -style fiber positioners within MOS instances. Most of these systems utilize either Faulhaber Precistep stepper motors or brushless DC motors with integral encoders, and these motors commonly have diameters starting from 6 mm upwards. The DESI project, uniquely, operates with a relatively small hollow-cup motor of  $\phi$ 4 mm. However, due to an absence of sensor feedback, the fiber positioner in DESI persists in employing an open-loop control strategy [14,30]. The advent of the micro magnetic encoder has enabled the realization of closed-loop control in hollow-cup motor-driven fiber positioners for the initial time. This control mode signifies a remarkable advancement over the open-loop method utilized by DESI, which operates without sensory feedback. The closed-loop system achieves a remarkable reduction in power consumption, merely utilizing 18.42% of the energy consumed by the precedent sensorless stepper motor strategy [29]. Considering the vast array of nearly ten thousand motors engaged simultaneously on a focal plane in a typical MOS, this energy efficiency is pivotal. It substantially abates the thermal effects imposed by the motor drive systems on the observational setting. Furthermore, the incorporation of angle sensors circumvents the persistent challenge of mechanical interference-caused motor blockages in parallel fiber positioning operations. Sensors allow for the rapid detection of such blockages, enabling the immediate shutdown of the motor to avoid damage. This advance promises lower maintenance frequency and downtime, making the system more resilient and reliable. Moreover, the implementation of angle sensors fosters angle-based closed-loop control that improves the precision of positioning in iterative tasks. It addresses the problem of step loss, a common issue in the stepper open-loop control mode, which can arise from blind movements. In the comprehensive visual servoing iterative framework, sensor-facilitated control demonstrates superior positioning and convergence performance, bolstering the accuracy and efficiency of the entire MOS.

**Table 2.** Overview of actuator characteristics for fiber positioners in MOS.

Fiber Positoner	Category	Actuator	Dimension	Control Mode	Supplier
LAMOST	$\theta$ - $\phi$	Stepper motor	$\phi$ 10 mm	Open-Loop	Faulhaber
MEGARA	$\theta$ - $\phi$	Stepper motor (3-line incremental encoder)	/	Open-Loop	Faulhaber
DESI	$\theta$ - $\phi$	BLDC	$\phi$ 4 mm	Open-Loop	Adamant Namiki
SDSS-V	$\theta$ - $\phi$	BLDC (Hall sensor)	$\phi$ 12 mm ( $\theta$ axis) $\phi$ 6 mm ( $\phi$ axis)	Closed-Loop	/
MOONS	$\theta$ - $\phi$	Stepper motor	$\phi$ 8 mm	Open-Loop	Faulhaber

Note: "/" indicates that relevant disclosure information has not been found or the feature does not exist.

While the current micro encoder system is limited to assembly solely on the central shaft motor, confining its application to prototype experiments, there remains considerable potential for enhancing its reliability and stability. A more efficient approach would be the integration of the micromagnetic encoder directly into the motor, creating a seamless and compact solution. This integration would substantially diminish the installation volume of the angle sensor, enabling its application in mechanisms with eccentric shafts. Moreover, a unified solution simplifies the installation process for workers and is more conducive to the mass production of fiber positioners. Ongoing discussions with motor manufacturers aim to explore potential collaborative opportunities to refine this integration. Prototype experiments are crucial for validating the principles of the system and evaluating

the control scheme's effectiveness. However, the benefits of mass production and the subsequent impact on system reliability and cost-effectiveness cannot be understated. Moving forward, it is anticipated that such experiments will lend greater credence to the viability of this technology in large-scale applications. Furthermore, the importance of micro-scale actuators and the miniaturization of instrumentation are becoming critical for a myriad of applications. Presently, for miniature hollow-cup motors with diminutive diameters of 4 mm, there is a notable absence of suitable position sensor solutions or servo control software and hardware from manufacturers. The newly developed 4 mm micro servo control system we present aims to bridge this gap, providing a holistic system-level solution to facilitate the utilization of these miniature motors in applications with spatial constraints. Our system is conceived to not only offer a solution for fiber positioners but also to drive the miniaturization trend in other instruments. The advancements in precision actuators and the concurrent design evolution in related hardware and software stand to benefit significantly from our system-level approach.

**Author Contributions:** Conceptualization, S.G.; Data curation, S.G.; Formal analysis, S.G. and Y.Y.; Funding acquisition, C.Z.; Investigation, S.G. and Y.Y.; Methodology, Y.Y.; Project administration, C.Z.; Resources, Y.Y.; Software, S.G.; Visualization, S.G.; Writing—review and editing, S.G. and Y.Y. All authors have read and agreed to the published version of the manuscript.

**Funding:** This research received no external funding.

**Data Availability Statement:** Data are contained within the article.

**Conflicts of Interest:** The authors declare no conflict of interest.

## References

1. Su, H.; Cui, X. LAMOST project and its current status. In *Large Ground-Based Telescopes, Proceedings of the Astronomical Telescopes and Instrumentation, Waikoloa, HI, USA, 22–23 August 2002*; Oschmann, J.M., Stepp, L.M., Eds.; International Society for Optics and Photonics, SPIE: Bellingham, WA, USA, 2003; Volume 4837, pp. 26–35. [[CrossRef](#)]
2. Iye, M. Overview of Subaru instrumentation. In *Optical Astronomical Instrumentation, Proceedings of the Astronomical Telescopes and Instrumentation, Kona, HI, USA, 9 July 1998*; D'Odorico, S., Ed.; International Society for Optics and Photonics, SPIE: Bellingham, WA, USA, 1998; Volume 3355, pp. 344–353. [[CrossRef](#)]
3. Edelstein, J.; Poppett, C.; Sirk, M.; Besuner, R.; Lafever, R.; Allington-Smith, J.R.; Murray, G.J. Optical fiber systems for the BigBOSS instrument. In *Modern Technologies in Space- and Ground-Based Telescopes and Instrumentation II, Proceedings of the SPIE Astronomical Telescopes + Instrumentation, Amsterdam, The Netherlands, 1–6 July 2012*; Navarro, R., Cunningham, C.R., Prieto, E., Eds.; International Society for Optics and Photonics, SPIE: Bellingham, WA, USA, 2012; Volume 8450, p. 845036. [[CrossRef](#)]
4. Jelinsky, P.; Bebek, C.; Besuner, R.; Carton, P.H.; Edelstein, J.; Lampton, M.; Levi, M.E.; Poppett, C.; Prieto, E.; Schlegel, D.; et al. The BigBOSS spectrograph. In *Ground-Based and Airborne Instrumentation for Astronomy IV, Proceedings of the SPIE Astronomical Telescopes + Instrumentation, Amsterdam, The Netherlands, 1–6 July 2012*; McLean, I.S., Ramsay, S.K., Takami, H., Eds.; International Society for Optics and Photonics, SPIE: Bellingham, WA, USA, 2012; Volume 8446, p. 844668. [[CrossRef](#)]
5. Schiavon, R.P.; Majewski, S.R. The Apache Point Observatory Galactic Evolution Experiment (APOGEE). *Proc. Int. Astron. Union* **2009**, *5*, 428–429. [[CrossRef](#)]
6. Hu, H.; Zhai, C.; Li, W.; Chen, H.; Chu, J.; Xing, X. Implementary scheme of parallel controllable optical fiber positioning system for LAMOST. In *Ground-Based and Airborne Instrumentation for Astronomy, Proceedings of the SPIE Astronomical Telescopes + Instrumentation, Orlando, FL, USA, 24–31 May 2006*; McLean, I.S., Iye, M., Eds.; International Society for Optics and Photonics, SPIE: Bellingham, WA, USA, 2006; Volume 6269, p. 62693A. [[CrossRef](#)]
7. Zhai, C.; Peng, X.; Xing, X. Observation planning of LAMOST fiber positioning subsystem and its simulation study. In *Large Ground-Based Telescopes, Proceedings of the Astronomical Telescopes and Instrumentation, Waikoloa, HI, USA, 22–28 August 2002*; Oschmann, J.M., Stepp, L.M., Eds.; International Society for Optics and Photonics, SPIE: Bellingham, WA, USA, 2003; Volume 4837, pp. 556–563. [[CrossRef](#)]
8. Silber, J.H.; Schenk, C.; Anderssen, E.; Bebek, C.; Becker, F.; Besuner, R.; Cepeda, M.; Edelstein, J.; Heetderks, H.; Jelinsky, P.; et al. Design and performance of an R-theta fiber positioner for the BigBOSS instrument. In *Modern Technologies in Space- and Ground-Based Telescopes and Instrumentation II, Proceedings of the SPIE Astronomical Telescopes + Instrumentation, Amsterdam, The Netherlands, 1–6 July 2012*; Navarro, R.; Cunningham, C.R.; Prieto, E., Eds.; International Society for Optics and Photonics, SPIE: Bellingham, WA, USA, 2012; Volume 8450, p. 845038. [[CrossRef](#)]

9. Makarem, L.; Kneib, J.P.; Gillet, D.; Bleuler, H.; Bouri, M.; Hörler, P.; Jenni, L.; Prada, F.; Sánchez, J. Collision-free motion planning for fiber positioner robots: Discretization of velocity profiles. In *Software and Cyberinfrastructure for Astronomy III, Proceedings of the SPIE Astronomical Telescopes + Instrumentation, Montréal, QC, Canada, 22–27 June 2014*; Chiozzi, G., Radziwill, N.M., Eds.; International Society for Optics and Photonics, SPIE: Bellingham, WA, USA, 2014; Volume 9152, p. 91520Q. [[CrossRef](#)]
10. Maihara, T.; Ohta, K.; Tamura, N.; Ohtani, H.; Akiyama, M.; Noumaru, J.; Kaifu, N.; Karoji, H.; Iye, M.; Dalton, G.B.; et al. Fiber multi-object spectrograph (FMOS) for the Subaru Telescope. In *Optical and IR Telescope Instrumentation and Detectors, Proceedings of the Astronomical Telescopes and Instrumentation, Munich, Germany, 27 March–1 April 2000*; Iye, M., Moorwood, A.F.M., Eds.; International Society for Optics and Photonics, SPIE: Bellingham, WA, USA, 2000; Volume 4008, pp. 1111–1118. [[CrossRef](#)]
11. Lang-Bardl, F.; Bender, R.; Grupp, F.; Häuser, M.; Hess, H.J.; Junk, V.; Kosyra, R.; Muschielok, B.; Richter, J.; Schlichter, J.; et al. A fibre positioner solution for the 4MOST instrument. In *Ground-Based and Airborne Instrumentation for Astronomy IV, Proceedings of the SPIE Astronomical Telescopes + Instrumentation, Amsterdam, The Netherlands, 1–6 July 2012*; McLean, I.S., Ramsay, S.K., Takami, H., Eds.; International Society for Optics and Photonics, SPIE: Bellingham, WA, USA, 2012; Volume 8446, p. 844661. [[CrossRef](#)]
12. Hörler, P.; Kronig, L.; Kneib, J.P.; Bouri, M.; Bleuler, H.; von Moos, D. High density fiber positioner system for massive spectroscopic surveys. *Mon. Not. R. Astron. Soc.* **2018**, *481*, 3070–3082. [[CrossRef](#)]
13. Pérez-Calpena, A.; Mancera, E.S.B.; Gomez-Alvarez, P.; Delgado, I.M.; Castillo, Á.; de Paz, A.G.; Arrillaga, X.; Vargas, M.L.G.; Gallego, J.; Licea, E.C.; et al. MEGARA MOS: Where are my positioners and fibers pointing to? In *Advances in Optical and Mechanical Technologies for Telescopes and Instrumentation III, Proceedings of the SPIE Astronomical Telescopes + Instrumentation, Austin, TX, USA, 10–15 June 2018*; Navarro, R., Geyl, R., Eds.; International Society for Optics and Photonics, SPIE: Bellingham, WA, USA, 2018; Volume 10706, p. 107062C. [[CrossRef](#)]
14. Leitner, D.; Aguilar, J.; Ameel, J.; Besuner, R.; Claybaugh, T.; Heetderks, H.; Schubnell, M.; Kneib, J.P.; Silber, J.; Tarlé, G.; et al. Dark energy spectroscopic instrument (DESI) fiber positioner production. In *Advances in Optical and Mechanical Technologies for Telescopes and Instrumentation III, Proceedings of the SPIE Astronomical Telescopes + Instrumentation, Austin, TX, USA, 10–15 June 2018*; Navarro, R., Geyl, R., Eds.; International Society for Optics and Photonics, SPIE: Bellingham, WA, USA, 2018; Volume 10706, p. 1070669. [[CrossRef](#)]
15. Cirasuolo, M.; Afonso, J.; Carollo, M.; Flores, H.; Maiolino, R.; Oliva, E.; Paltani, S.; Vanzi, L.; Evans, C.; Abreu, M.; et al. MOONS: The Multi-Object Optical and Near-infrared Spectrograph for the VLT. In *Ground-Based and Airborne Instrumentation for Astronomy V, Proceedings of the SPIE Astronomical Telescopes + Instrumentation, Montréal, QC, Canada, 22–27 June 2014*; Ramsay, S.K., McLean, I.S., Takami, H., Eds.; International Society for Optics and Photonics, SPIE: Bellingham, WA, USA, 2014; Volume 9147, p. 91470N. [[CrossRef](#)]
16. Fahim, N.; Prada, F.; Kneib, J.P.; Glez-de Rivera, G.; Hörler, P.; Sánchez, J.; Azzaro, M.; Becerril, S.; Bleuler, H.; Bouri, M.; et al. An 8-mm diameter fibre robot positioner for massive spectroscopy surveys. *Mon. Not. R. Astron. Soc.* **2015**, *450*, 794–806. [[CrossRef](#)]
17. Araujo, R.; Bouri, M.; Brandon, C.; Caseiro, S.; Gillet, D.; Grossen, L.; Kronig, L.; Macktoobian, M.; O'Brien, T.; Pogge, R.W.; et al. Design of a Theta/Phi fiber positioner robot for the Sloan Digital Sky Survey V. In *Ground-Based and Airborne Instrumentation for Astronomy VIII, Proceedings of the SPIE Astronomical Telescopes + Instrumentation, Online Only, 14–18 December 2020*; Evans, C.J., Bryant, J.J., Motohara, K., Eds.; International Society for Optics and Photonics, SPIE: Bellingham, WA, USA, 2020; Volume 11447, p. 1144790. [[CrossRef](#)]
18. Haeuser, M.; Lang-Bardl, F.; Richter, J.; Hess, H.J.; Degwert, A.; Karasz, A.; Kosyra, R.; Hopp, U.; Bender, R. Presenting a high accuracy Theta-Phi-style fiber-positioner prototype with a 15-mm pitch. In *Ground-Based and Airborne Instrumentation for Astronomy V, Proceedings of the SPIE Astronomical Telescopes + Instrumentation, Montréal, QC, Canada, 22–27 June 2014*; Ramsay, S.K., McLean, I.S., Takami, H., Eds.; International Society for Optics and Photonics, SPIE: Bellingham, WA, USA, 2014; Volume 9147, p. 91476V. [[CrossRef](#)]
19. Jansen, P.; Lorenz, R. Transducerless position and velocity estimation in induction and salient AC machines. *IEEE Trans. Ind. Appl.* **1995**, *31*, 240–247. [[CrossRef](#)]
20. Kim, S.I.; Im, J.H.; Song, E.Y.; Kim, R.Y. A New Rotor Position Estimation Method of IPMSM Using All-Pass Filter on High-Frequency Rotating Voltage Signal Injection. *IEEE Trans. Ind. Electron.* **2016**, *63*, 6499–6509. [[CrossRef](#)]
21. Corley, M.; Lorenz, R. Rotor position and velocity estimation for a salient-pole permanent magnet synchronous machine at standstill and high speeds. *IEEE Trans. Ind. Appl.* **1998**, *34*, 784–789. [[CrossRef](#)]
22. Zhang, G.; Wang, G.; Wang, H.; Xiao, D.; Li, L.; Xu, D. Pseudorandom-Frequency Sinusoidal Injection Based Sensorless IPMSM Drives With Tolerance for System Delays. *IEEE Trans. Power Electron.* **2019**, *34*, 3623–3632. [[CrossRef](#)]
23. Masaki, R.; Kaneko, S.; Hombu, M.; Sawada, T.; Yoshihara, S. Development of a position sensorless control system on an electric vehicle driven by a permanent magnet synchronous motor. In *Proceedings of the Power Conversion Conference-Osaka 2002 (Cat. No. 02TH8579)*, Osaka, Japan, 2–5 April 2002; Volume 2, pp. 571–576. [[CrossRef](#)]
24. Wang, G.; Xiao, D.; Zhang, G.; Li, C.; Zhang, X.; Xu, D. Sensorless Control Scheme of IPMSMs Using HF Orthogonal Square-Wave Voltage Injection Into a Stationary Reference Frame. *IEEE Trans. Power Electron.* **2019**, *34*, 2573–2584. [[CrossRef](#)]
25. Allotta, B.; Pugi, L.; Paolucci, L.; D'Adamio, P.; Nocentini, L.; Niehaus, M.; Grasso, E.; Kanapari, E. Development of sensorless PM servo-system for harsh environments. In *Proceedings of the 2015 AEIT International Annual Conference (AEIT)*, Naples, Italy, 14–16 October 2015; pp. 1–6. [[CrossRef](#)]
26. Naderian, M.; Markadeh, G.A.; Karimi-Ghartemani, M.; Mojiri, M. Improved Sensorless Control Strategy for IPMSM Using an ePLL Approach With High-Frequency Injection. *IEEE Trans. Ind. Electron.* **2024**, *71*, 2231–2241. [[CrossRef](#)]

27. Yao, X.; Wang, Y.; Huang, S.; Zhang, G.; Ma, H. Modified ESO-Based Back EMF Estimation and Rotor Position Extraction Method for SPMSM Sensorless Control. In Proceedings of the IECON 2023-49th Annual Conference of the IEEE Industrial Electronics Society, Singapore, 16–19 October 2023; pp. 1–6. [[CrossRef](#)]
28. Lee, J.; Hong, J.; Nam, K.; Ortega, R.; Praly, L.; Astolfi, A. Sensorless Control of Surface-Mount Permanent-Magnet Synchronous Motors Based on a Nonlinear Observer. *IEEE Trans. Power Electron.* **2010**, *25*, 290–297. [[CrossRef](#)]
29. Guo, S.X.; Zhai, C.; Bi, S.L. Low voltage optical fiber positioner robot based on minimum inductance hollow cup motors. *Sci. Rep.* **2022**, *12*, 2705. [[CrossRef](#)] [[PubMed](#)]
30. Schubnell, M.; Ameel, J.; Besuner, R.W.; Gershkovich, I.; Hoerler, P.; Kneib, J.P.; Heetderks, H.D.; Silber, J.H.; Tarlé, G.; Weaverdyck, C. The DESI fiber positioner system. In *Ground-Based and Airborne Instrumentation for Astronomy VI, Proceedings of the SPIE Astronomical Telescopes + Instrumentation, Edinburgh, UK, 26 June–1 July 2016*; Evans, C.J., Simard, L., Takami, H., Eds.; International Society for Optics and Photonics, SPIE: Bellingham, WA, USA, 2016; Volume 9908, p. 990892. [[CrossRef](#)]

**Disclaimer/Publisher’s Note:** The statements, opinions and data contained in all publications are solely those of the individual author(s) and contributor(s) and not of MDPI and/or the editor(s). MDPI and/or the editor(s) disclaim responsibility for any injury to people or property resulting from any ideas, methods, instructions or products referred to in the content.